



HAL
open science

Flow features near plate impinged by ideally expanded and underexpanded round jets

Romain Gojon, Christophe Bogey

► **To cite this version:**

Romain Gojon, Christophe Bogey. Flow features near plate impinged by ideally expanded and underexpanded round jets. *AIAA Journal*, 2018, 56, pp.445-457. 10.2514/1.J056421 . hal-02085849

HAL Id: hal-02085849

<https://hal.science/hal-02085849v1>

Submitted on 18 Oct 2024

HAL is a multi-disciplinary open access archive for the deposit and dissemination of scientific research documents, whether they are published or not. The documents may come from teaching and research institutions in France or abroad, or from public or private research centers.

L'archive ouverte pluridisciplinaire **HAL**, est destinée au dépôt et à la diffusion de documents scientifiques de niveau recherche, publiés ou non, émanant des établissements d'enseignement et de recherche français ou étrangers, des laboratoires publics ou privés.

Flow features near the plate impinged by ideally-expanded and underexpanded round jets

Romain Gojon^{1,*} and Christophe Bogey^{2,†}

1. *Department of Mechanics, Royal Institute of Technology (KTH)*

Linné FLOW Centre

Stockholm, Sweden

2. *Laboratoire de Mécanique des Fluides et d'Acoustique,*

UMR CNRS 5509, Ecole Centrale de Lyon, Université de Lyon,

69134 Ecully Cedex, France

The properties of the flow near the plate and in the wall jets have been investigated from large eddy simulation data of round impinging jets. Four jets are under-expanded, and four jets are ideally expanded, which allowed us to examine the influence of the presence of shock-cell structures. The under-expanded jets are characterized by a fully-expanded Mach number of 1.56 and an exit Mach number of 1. The ideally-expanded jets have a Mach number of 1.5. The Reynolds number of the eight jets is equal to 6×10^4 . The jets impinge normally on a flat plate located from $4.16r_0$ to $12r_0$ downstream of the nozzle, and generate acoustic tones due to an aeroacoustic feedback mechanism. In this paper, the near pressure and density fields of the jets are characterized using Fourier Transform on the nozzle-exit plane, the plate, and an azimuthal plane. First, mean and rms radial velocities of the wall jets are examined. The impact of the shock-cell structure on the wall jet is discussed. The pressure spectra on the plate are then shown as a function of the radial coordinate. The tone frequencies are all visible where the jet shear layers impinge the plate, but only some of them emerge in the wall jet created after the impact. For the ideally-expanded jets, the temporal organization of the wall jet along the frequencies of the feedback mechanism decreases with the nozzle-to-plate distance, but for the non-ideally expanded jets, this organization is linked to the oscillation of the Mach disk located just upstream of the

*PostDoc, AIAA Member, gojon@kth.se

†Research Scientist, Senior Member AIAA, christophe.bogey@ec-lyon.fr

plate. Consecutively, the amplitude and the phase fields at the tone frequencies are represented on the three planes mentioned earlier. Similar spatial organizations of the turbulent structures are found in the jet shear layers and in the wall jets. Thus, axisymmetric and helical arrangements of the structures in the jet shear layers lead to concentric and spiral distributions of the structures on the plate, respectively. In particular, for one of the under-expanded jets, a spiral shape and concentric rings, associated with two tone frequencies generated simultaneously, are observed on the flat plate in the pressure and density phase fields. Finally, the convection velocity of the turbulent structures at the tone frequencies in the wall jets are evaluated based on phase fields, and the mean convection velocity is computed using cross-correlations of radial velocity. The results are in good agreement with those from a recent experimental study of ideally expanded impinging jets.

Nomenclature

a_e	=	speed of sound at the nozzle exit (m/s)
a_j	=	speed of sound in the ideally expanded equivalent jet (m/s)
D	=	diameter of the jet (m)
D_j	=	diameter of the ideally expanded equivalent jet (m)
f	=	frequency (Hz)
L	=	nozzle-to-plate distance (m)
$\mathcal{M}_e = u_e/a_e$	=	exit Mach number
\mathcal{M}_j	=	Mach number of the ideally expanded equivalent jet
u_c	=	convection velocity (m/s)
u_e	=	velocity at the nozzle exit (m/s)
u_j	=	velocity of the ideally expanded equivalent jet (m/s)
r_0	=	radius of the jet (m)
$St = fD_j/u_j$	=	Strouhal number

I. Introduction

High-subsonic and supersonic jets impinging on a flat plate have been studied by many researchers during the past decades, notably by Powell¹ and Wagner.² Very intense tones have been observed in the acoustic field. Powell¹ suggested that such tones are generated by an aeroacoustic feedback mechanism involving the turbulent structures propagating downstream from the nozzle to the plate and the acoustic waves propagating

upstream from the plate to the nozzle.

For subsonic impinging round jets, the tone frequencies are well predicted by the model proposed by Ho & Nosseir³ and Nosseir & Ho.⁴ Round supersonic jets impinging on a flat plate normally have been investigated experimentally by Henderson & Powell,⁵ Krothapalli *et al.*⁶ and Henderson *et al.*,⁷ among others. In some cases, a feedback mechanism is observed as in subsonic jets. This is very often the case when the jet is ideally expanded, but this happens only for some nozzle-to-plate distances when the jet is imperfectly expanded. In the latter case, Henderson & Powell⁵ suggested that the feedback loop establishes only when a Mach disk forms just upstream from the plate. More recently, for underexpanded impinging jets, Risbord & Soria⁸ explored the instability modes of the jets using ultra-high-speed Schlieren and shadowgraph techniques. Notably, axial and helical modes were visualized, and the Mach disk located just upstream from the plate was found to oscillate. For similar jets, Buchmann *et al.*⁹ pointed out the periodic formation of large-scale structures in the jet shear layers using a high spatial resolution Schlieren imaging. The complete feedback mechanism, including large-scale structures in the shear layers propagating downstream from the nozzle to the plate and acoustic waves propagating upstream from the plate to the nozzle, was visible. Mitchell *et al.*¹⁰ studied the periodic oscillations of the shear layer of under-expanded impinging jets using time-resolved Schlieren image sequences.

For under-expanded impinging jets, the presence of recirculation zones near the plate and the dynamic of the fluid between the Mach disk created just upstream of the plate and the plate was investigated experimentally by Henderson *et al.*⁷ Notably, tones were found to be produced in the peripheral supersonic flow. Recirculation zones were also observed between the near-wall Mach disk and the flat plate for some nozzle-to-plate distances by Krothapalli *et al.*⁶ Kuo and Dowling¹¹ derived a model considering pressure waves and entropy fluctuations in order to explain the oscillation modes of the jet at the feedback tone frequencies. Numerically, Dauplain *et al.*^{12,13} proposed a new path for the aeroacoustic feedback mechanism passing through the wall jet created after the jet impact. More recently, Weightman *et al.*¹⁴ analyzed the dynamic of the creation of an acoustic wave at the plate surface using ultra-high-speed schlieren. Finally, Davis *et al.*¹⁵ studied the wall pressure oscillations in ideally expanded impinging jets using a fast-response Pressure-Sensitive Paint on the plate. They identified axisymmetrical and helical oscillation modes of the jets associated with tone frequencies thanks to phase-conditioned Schlieren images. For such modes, they presented the phase-averaged distributions of the fluctuating pressure on the flat plate. The turbulent structures organized axisymmetrically or helically in the jet shear layers were shown to persist after the impact, as they propagate radially in the wall jets, even several diameters away from the jet axis. The turbulent organization in the wall jet created after the impact is thus of primary interest to gain insights on the flow and acoustic properties of supersonic impinging jets. However, it has rarely been described in the past,

notably because of experimental difficulties to perform measurements in this region with PIV techniques due to the reflections coming from the plate. This is fortunately not the case using recent fast-response Pressure-Sensitive Paint. Indeed, Davis *et al.*¹⁵ can reach a frequency resolution of several kHz , permitting to study mechanisms like the feedback loop establishing in supersonic impinging jets.

In previous studies by the authors,^{16,17} the feedback loop and the associated oscillations of the jets have been studied. In this paper, the azimuthal organization of turbulent structures in the jet shear layers and on the flat plate, in the wall jets created after the impact, are characterized from data provided by large eddy simulations. The aerodynamic and acoustic properties of the eight jets have been detailed previously in Gojon *et al.*¹⁶ for the non-ideally expanded jets and in Bogey and Gojon¹⁷ for the ideally expanded jets. The spatial organization and the convection velocity of the turbulent structures in the wall jet are examined from the pressure and density fields on the plate. The effects of the presence of shock-cell structures are sought. The paper is organized as follows. The jet conditions and the numerical parameters are presented in section II. Snapshots of two jets and the properties of the aeroacoustic feedback loop establishing in the jets are provided in section III. In section IV, the mean and rms fields of the radial velocity in the wall jets are shown. An analysis of the turbulent structures in the jet shear layers and in the wall jets is also conducted by plotting the amplitude and phase fields of the pressure and density fields at the tone frequencies. Concluding remarks are finally given in section V.

II. Parameters

II.A. Jet conditions

In this section, the main jet conditions are provided. More informations can be found in previous papers.^{16,17} The jets have a Temperature Ratio $TR = T_r/T_{amb} = 1$, where T_r and T_{amb} are the stagnation and the ambient temperatures. They originate from a pipe nozzle of radius r_0 , whose lip is $0.1r_0$ thick. At the nozzle inlet, a Blasius mean velocity profile is imposed with a boundary-layer thickness of $0.15r_0$.

For the ideally expanded jets, the nozzle-to-plate distances L are respectively equal to $6r_0$, $8r_0$, $10r_0$ and $12r_0$, as shown in table 1. The jets are thus referred to as JetidealL6, JetidealL8, JetidealL10 and JetidealL12. They have an exit Mach number of $\mathcal{M}_e = u_e/a_e = 1.5$, where u_e and a_e are the exit velocity and the speed of sound in the jet, and a Reynolds number of $Re_j = u_e D/\nu = 6 \times 10^4$, where $D = 2r_0$ is the nozzle diameter and ν is the kinematic molecular viscosity. The jet ejection conditions and the nozzle-to-plate distances are identical to those in the experimental study of Krothapalli *et al.*,⁶ whereas the jet Reynolds number is one order of magnitude lower than the experimental one.

For the non-ideally expanded jets, the nozzle-to-plate distances L are equal to $4.16r_0$, $5.6r_0$, $7.3r_0$ and $9.32r_0$, see also in table 1. The jets are thus denoted as JetunderL4, JetunderL5, JetunderL7 and JetunderL9.

They have an ideally expanded Mach number of $\mathcal{M}_j = u_j/a_j = 1.56$, where u_j and a_j are the exit velocity and the speed of sound in the ideally-expanded equivalent jet. Their Reynolds number is $Re_j = u_j D_j/\nu = 6 \times 10^4$, where D_j is the nozzle diameter of the ideally expanded equivalent jet. The exit Mach number is $\mathcal{M}_e = 1$. The ejection conditions of the jets and the nozzle-to-plate distances are identical to those in the experiments of Henderson *et al.*,⁷ and the jet Reynolds number is one order of magnitude lower than the experimental one.

II.B. Numerical parameters

In the LES, the unsteady compressible Navier-Stokes equations are solved on cylindrical meshes (r, θ, z) using an explicit six-stage Runge-Kutta algorithm for time integration, and low-dissipation and low-dispersion explicit eleven-point finite differences for spatial derivation.^{18,19} At the end of each time step, a high-order filtering is applied to the flow variables in order to remove grid-to-grid oscillations and to dissipate subgrid-scale turbulent energy.^{20–22} The radiation conditions of Tam & Dong²³ are implemented at the boundaries of the computational domain, in combination with a sponge zone at the outflow boundaries combining grid stretching and Laplacian filtering to damp turbulent fluctuations and acoustic waves before they reach the boundaries. Adiabatic no-slip conditions are imposed at the nozzle walls and at the flat plate. Finally, a shock-capturing filtering is applied in order to avoid Gibbs oscillations near shocks.²⁴ The axis singularity is treated with the method proposed by Mohseni & Colonius.²⁵ A reduction of the effective resolution near the origin of the polar coordinates is also implemented.²⁶ Finally, a forcing²⁷ is added in the boundary layer in the nozzle in order to generate velocity fluctuations at the nozzle exit. This procedure enables to reach peak turbulent intensities between 2.6% for JetidealL12 and 7.3% for JetunderL4.

The simulations are carried out using an OpenMP-based in-house solver, and a total of 250,000 or more iterations are performed in each case after the transient period. The simulation time is equal to $1250r_0/u_j$ or more. The cylindrical meshes contain between 171 and 240 million points, as reported in Table 1. The minimal axial mesh spacing, equal to $\Delta z = 0.0075r_0$, is located near the nozzle lip and the flat plate, and the maximal axial mesh spacing, equal to $\Delta z = 0.03r_0$, is located between the nozzle and the plate. The minimal radial spacing is equal to $\Delta r = 0.0075r_0$ at $r = D/2$, and the maximal radial spacing, excluding the sponge zone, is $\Delta r = 0.06r_0$ for $5r_0 \leq r \leq 15r_0$. The maximum mesh spacing of $0.06r_0$ allows acoustic waves with Strouhal numbers up to $St = fD_j/u_j = 5.3$ to be well propagated in the computational domains, where f is the frequency. Thus, the computational domain, excluding the sponge zones, extends from $6r_0$ upstream of the nozzle exit to the plate in the axial direction and from $-15r_0$ to $15r_0$ in the radial direction. A complete description of the meshes can be found in the previous papers.^{16,17}

The discretization of the wall jet forming after the jet impact is analysed at $r = 4r_0$. In the directions

	L	n_r	n_θ	n_z	number of points
JetidealL6	$6r_0$	500	512	791	202×10^6
JetidealL8	$8r_0$	500	512	803	205×10^6
JetidealL10	$10r_0$	500	512	869	222×10^6
JetidealL12	$12r_0$	500	512	936	240×10^6
JetunderL4	$4.16r_0$	500	512	668	171×10^6
JetunderL5	$5.6r_0$	500	512	764	195×10^6
JetunderL7	$7.3r_0$	500	512	780	200×10^6
JetunderL9	$9.32r_0$	500	512	847	217×10^6

Table 1. Mesh parameters: nozzle-to-plate distance L , number of points n_r , n_θ and n_z in the radial, azimuthal and axial directions, and total number of points.

parallel to the wall, values of about $\Delta r^+ \simeq r\Delta\theta^+ \simeq 30$ are found for the four jets. Those values are similar to those used in the literature for the LES of turbulent boundary layers.²⁸⁻³⁰ In the direction normal to the wall, values $\Delta z^+ \simeq 5$ are used. This value do not permit in theory to simulate with accuracy the turbulent boundary layer of the wall jet. However, using a similar solver, Bogey and Marsden³¹ showed for the turbulent boundary layer developing in the nozzle of a turbulent subsonic jet that the LES results do not depend significantly on the mesh spacing in the direction normal to the wall for values $\Delta^+ = 3.7$ and below.

III. Feedback loop

III.A. Snapshots

Three- and two-dimensional snapshots are represented in Figures 1 and 2 for JetidealL6 and JetunderL7, respectively. For the 3-D snapshots, in order to visualize both the flow and the acoustic fields of the jets, isosurfaces of density and pressure fields in the plane $\theta = 0$ are shown. For the 2-D snapshots, the density is represented in the jet and near the wall and the the pressure field is displayed everywhere else.

The development of the jet shear layers are well visible and exhibit both large-scale and small-scale turbulent structures, in agreement with the Reynolds number of 6×10^4 . In the pressure fields, acoustic waves coming from the region of jet impact and propagating in the upstream direction, are noticed. In the 2-D snapshots, the density fields reveal the difference between JetidealL6, which is an ideally expanded jet with no shock cell structure and JetunderL7, which is an underexpanded jet with two shock cells visible. In the present study, the wall jets created after the jet impact, well visible on the 3-D snapshots, are studied.

III.B. Tone frequencies

The pressure spectra obtained at $z = 0$ and $r = 2r_0$ for the two cases whom snapshots are given in Sec. III.A, JetidealL6 and JetunderL7, are displayed in figure 3 as functions of the Strouhal number $St = fD_j/u_j$. In

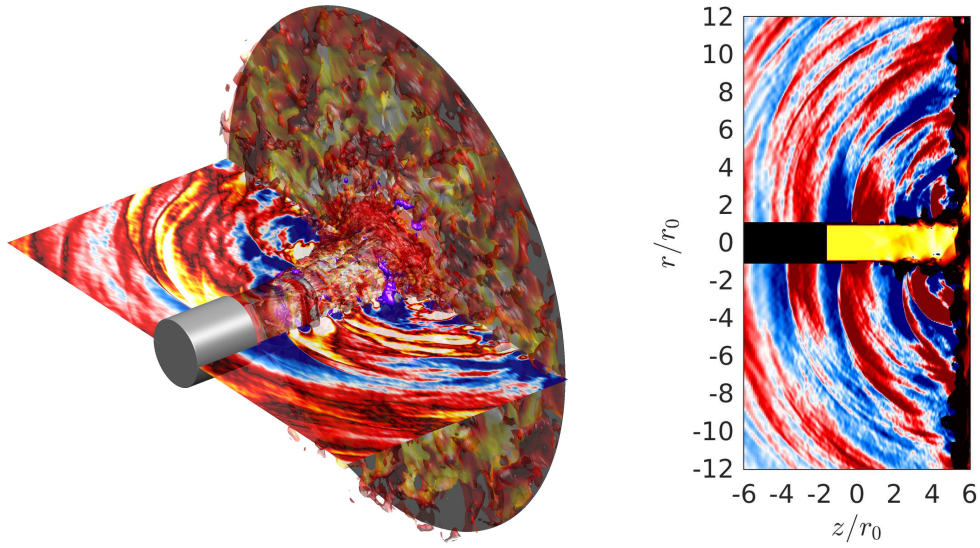


Figure 1. Representation, for JetidealL6, of (a) isosurfaces of $1.3 \text{ kg}\cdot\text{m}^{-3}$, colored by the Mach number; and the pressure field in the plane $\theta = 0$, (b) snapshot in the (z, r) plane of the density in the jets and close to the flat plate and of the pressure fluctuations. The colour scale ranges from 1 to $2 \text{ kg}\cdot\text{m}^{-3}$ for the density and from -5000 to 5000 Pa for the fluctuating pressure.

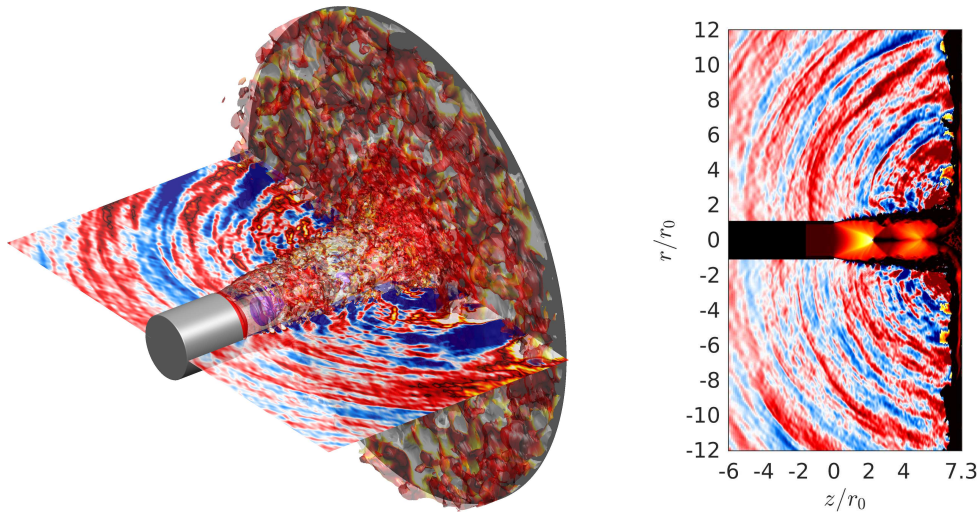


Figure 2. Representation, for JetunderL7 of (a) isosurfaces of density, the violet and red isosurfaces for the values of 0.95 and $2 \text{ kg}\cdot\text{m}^{-3}$, respectively, isosurfaces of $1.25 \text{ kg}\cdot\text{m}^{-3}$ colored by the Mach number; and the pressure field in the plane $\theta = 0$, (b) snapshot in the (z, r) plane of the density in the jets and close to the flat plate and of the pressure fluctuations. The colour scale ranges from 1 to $2 \text{ kg}\cdot\text{m}^{-3}$ for the density and from -5000 to 5000 Pa for the fluctuating pressure.

Figure 3(a), about ten tone frequencies are visible for JetidealL6, between $St = 0.2$ and $St = 2$ whereas only three can be seen for JetunderL7 in Figure 3(b).

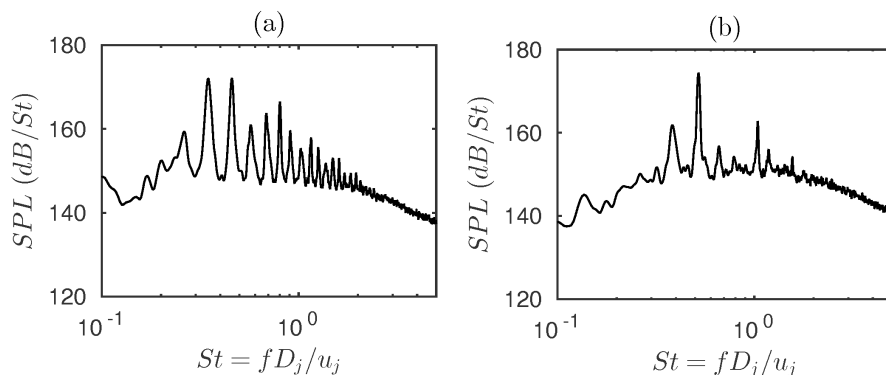


Figure 3. Sound pressure levels at $r = 2r_0$ and $z = 0$ as functions of the Strouhal number $St = fD_j/u_j$ for (a) JetidealL6 and (b) JetunderL7.

For the other jets, the sound pressure levels obtained in the vicinity of the nozzle also reveal several tone frequencies.^{16,17} The first four Strouhal numbers of the tones whose levels are 5 dB higher than the broadband noise are reported in table 2. The tones are generated by an aeroacoustic feedback mechanism occurring between the nozzle and the plate. A good agreement has been found between the tone frequencies of the present simulated jet, those found in the experimental studies of Henderson *et al.*⁷ and Krothapalli *et al.*,⁶ and the frequencies predicted by the classical feedback model.^{3,4} The corresponding comparisons are available in previous papers.^{16,17}

	St_1	St_2	St_3	St_4
JetidealL6	0.26	0.345	0.455	0.57
JetidealL8	0.205	0.29	0.365	0.445
JetidealL10	0.165	0.29	0.375	0.44
JetidealL12	0.175	0.255	0.305	0.38
JetunderL4	0.375	0.505	1.01	-
JetunderL5	0.335	0.415	-	-
JetunderL7	0.345	0.42	-	-
JetunderL9	0.27	0.34	0.42	-

Table 2. Strouhal numbers emerging in the pressure spectra in the vicinity of the nozzle. The Strouhal numbers of the dominant tones are in bold.

Overall, for the ideally expanded jets, about ten tones are noticed, as observed for ideally expanded planar supersonic jets experimentally³² and numerically.³³ On the contrary, only two or three dominant tones are found for the non-ideally expanded jets, as already noted in various experimental studies.^{6,7,34,35}

For each of these tone frequencies, the corresponding axisymmetric or helical jet oscillation and the associated mode number in the classical model proposed by Ho & Nosseir³ and Nosseir & Ho⁴ have been identified.^{16,17} The results are given in Table 3, and they will be used in the next sections.

	St_1	St_2	St_3	St_4
JetidealL6	$N = 2$, hel.	$N = 3$, hel.	$N = 4$, axi.	$N = 5$, hel.
JetidealL8	$N = 2$, axi.	$N = 3$, hel.	$N = 4$, axi.	$N = 5$, axi.
JetidealL10	$N = 2$, axi.	$N = 4$, hel.	$N = 5$, axi.	$N = 6$, axi.
JetidealL12	$N = 3$, axi.	$N = 4$, hel.	$N = 5$, hel.	$N = 6$, axi.
JetunderL4	$N = 2$, hel.	$N = 3$, axi.	-	-
JetunderL5	$N = 2$, hel.	$N = 3$, hel.	-	-
JetunderL7	$N = 3$, hel.	$N = 4$, hel.	-	-
JetunderL9	$N = 3$, hel.	$N = 4$, hel.	$N = 5$, hel.	-

Table 3. Mode number and oscillation nature of the jet oscillations at the first four tone Strouhal numbers. The terms hel. or axi. denote helical and axisymmetric.

IV. Flow properties near the flat plate

This section deals with the flow properties in the wall jet region, where no experimental data are available. Comparisons of mean fields and turbulent levels with experimental data in the jets are available in previous papers.^{16,17}

IV.A. Flow field statistics

The mean radial velocities obtained for the four ideally-expanded jets are represented in Figure 4, where z_w is the axial location of the plate. The wall jets are created at $r \sim r_0$, where the jet shear layers impinge on the plate. The peak radial velocities of the wall jets are equal to $0.913u_j$ for JetidealL6, $0.870u_j$ for JetidealL8, $0.847u_j$ for JetidealL10, and $0.820u_j$ for JetidealL12. As expected, the larger the nozzle-to-plate distance, the lower the maximum radial velocity in the wall jet.

The rms values of the radial velocity fluctuations are displayed in Figure 5 for the four ideally expanded jets. The jet shear layers and the wall jets both appear clearly. Higher values are found in the wall jets than in the jet shear layers. The maximal values in the wall jets decrease with the nozzle-to-plate distance, yielding $0.232u_j$ for JetidealL6, $0.209u_j$ for JetidealL8, $0.193u_j$ for JetidealL10, and $0.180u_j$ for JetidealL12. The position where the maximal value is reached varies from $2.1r_0$ for JetidealL6 up to $4.0r_0$ for JetidealL12.

The mean radial velocity of the four non-ideally expanded jets are shown in Figure 6. The shock cell structures of the jets are visible, leading to positive and negative values of the mean radial velocity. The presence of the shock cell structure results in the formation of a recirculation bubble near the plate, at $r \sim r_0$, visible thanks to the isocontour for $\langle u_r \rangle = -0.05u_j$ in Figure 6. Moreover, in this case, the variation of the maximal value of the mean radial velocity with the nozzle-to-plate distance is not monotonous, and they are equal to $0.897u_j$ for JetunderL4, $0.956u_j$ for JetunderL5, $0.963u_j$ for JetunderL7 and $0.893u_j$ for JetunderL9. Finally, using isocontours for $\langle u_r \rangle = 0.9u_j$, shock cells appear in the wall jet for JetunderL5 and JetunderL7, for which the highest mean radial velocities are found. For those two jets, the cylindrical

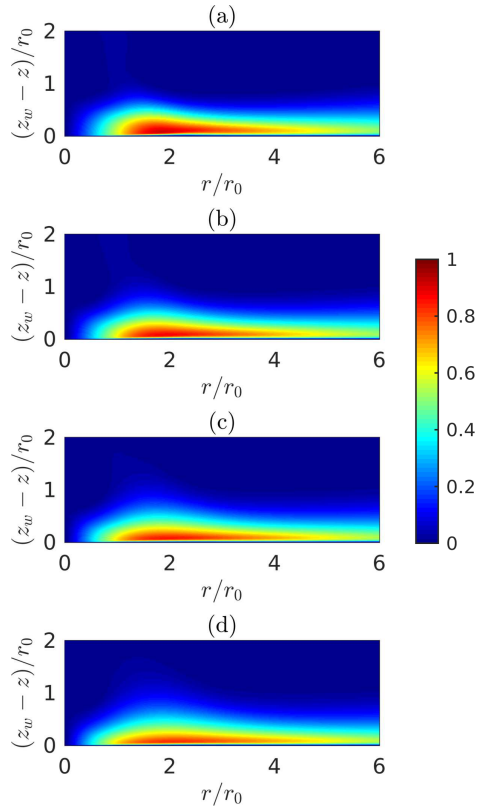


Figure 4. Mean radial velocity $\langle u_r \rangle / u_j$ for (a) JetidealL6, (b) JetidealL8, (c) JetidealL10 and (d) JetidealL12.

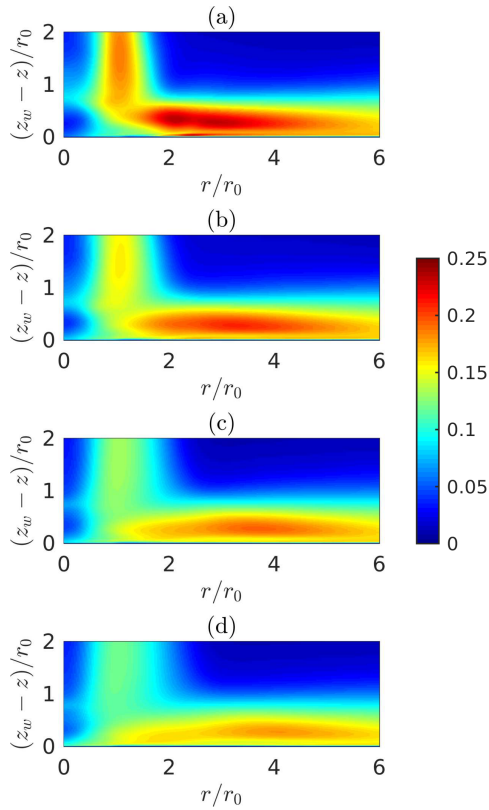


Figure 5. Rms values of radial velocity fluctuations $u_{r,rms} / u_j$ for (a) JetidealL6, (b) JetidealL8, (c) JetidealL10 and (d) JetidealL12.

wall jet is thus organized with annular shock cell structures.

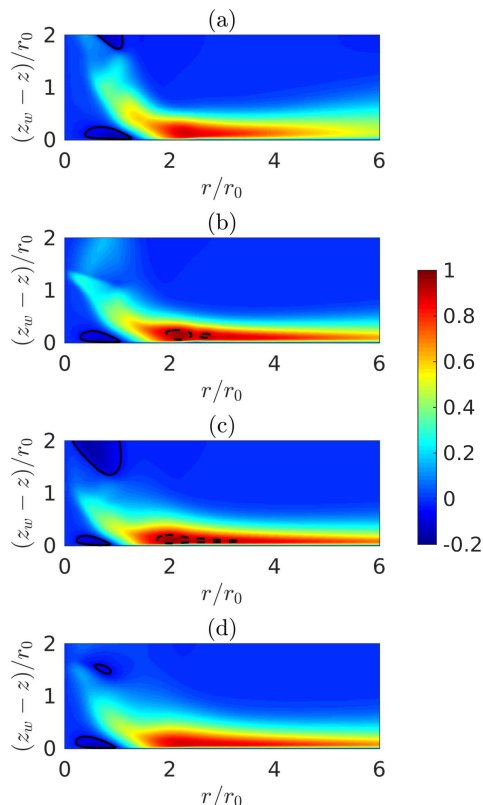


Figure 6. Mean radial velocity $\langle u_r \rangle / u_j$ for (a) JetunderL4, (b) JetunderL5, (c) JetunderL7 and (d) JetunderL9; — isocontour for $\langle u_r \rangle = -0.05u_j$ and - - - isocontour for $\langle u_r \rangle = 0.9u_j$.

For the four under-expanded jets, the rms values of radial velocity fluctuations are represented in Figure 7. For JetunderL4, JetunderL5 and JetunderL9, the Mach disk formed just upstream from the plate¹⁶ is visible. Downstream from the Mach disk, a shear layer is created in the jet and spreads to the wall by expanding in the radial direction, creating a conical area of high turbulence intensity. This area represents the recirculation bubble with flow moving from the position where the jet shear layers impinge on the plate to the center of the Mach disk, about one radius upstream from the plate. In the wall jets, the maximal rms value of the radial velocity decreases with the nozzle-to-plate distance, and is equal to $0.226u_j$ for JetunderL4, $0.195u_j$ for JetunderL5, $0.191u_j$ for JetunderL7 and $0.182u_j$ for JetunderL9.

Overall, for the ideally expanded jets, the maximal mean and rms values of the radial velocity in the wall jets decrease with the nozzle-to-plate distance, as expected. However, for the under-expanded jets, the presence of the shock cell structure appears to affect the maximal mean velocity in the wall jet. Indeed, the highest value is found for JetunderL7, for which there is no Mach disk just upstream of the plate.¹⁶ The presence of the oblique shock just upstream of the plate in JetunderL7 thus seems to enable the jet shear layer to deviate and become a wall jet, leading to high velocity speeds close to the wall.

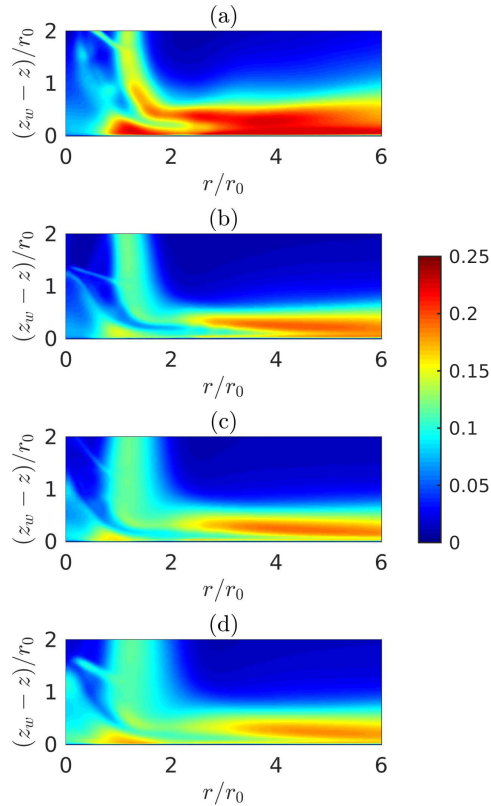


Figure 7. Rms values of radial velocity fluctuations $u_{r,rms}/u_j$ for (a) JetunderL4, (b) JetunderL5, (c) JetunderL7 and (d) JetunderL9.

IV.B. Pressure and density fields on the plate

IV.B.1. Snapshots

During the LES, pressure has been recorded in the planes $z = 0$, $z = L$ and $\theta = 0$. Moreover, density has also been stored in the plane $z = L$. A Fourier decomposition of the fields is carried out, permitting to plot the amplitude and phase fields for a given frequency.

Snapshots of the density and pressure fields obtained at the wall for the ideally expanded jets are presented in Figure 8. A movie showing the temporal evolution of the fields is also available online. In the density fields, high values are found at the center of the domain, in the region of jet impact. Turbulent structures coming from the jet shear layers are observed to propagate radially in the movie. In the pressure fields, the exact location of the jet impact clearly appears. It is not perfectly round nor centered. Turbulent structures propagating radially can be also be seen. The larger area of the jet impact in the density field than in the pressure fields is most likely due to the fact that the jet is cold.

Density and pressure snapshots are represented in Figure 9 for the four under-expanded jets, and a corresponding movie is given online. In the density field, low values of density are found around $r = 0$. This results from the presence of a shock cell structure, see in Figure 2(b). Turbulent structures from the jet shear

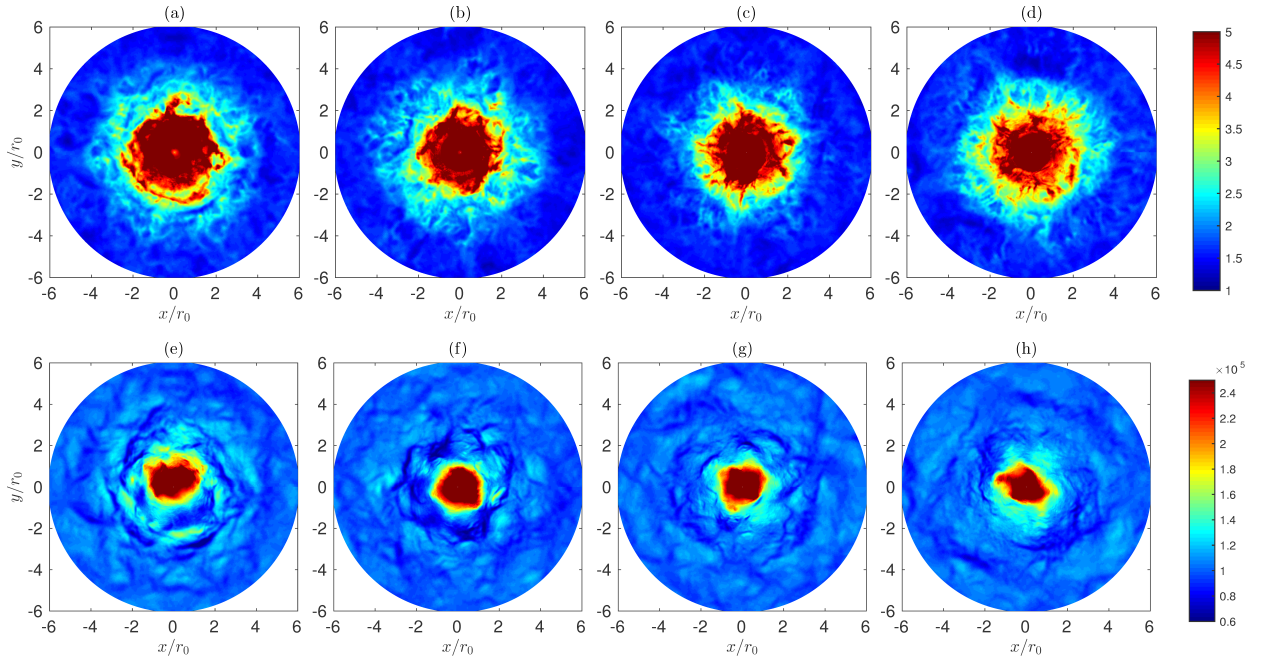


Figure 8. Density (top) and pressure (bottom) fields on the plate obtained for (a,e) JetidealL6, (b,f) JetidealL8, (c,g) JetidealL10 and (d,h) JetidealL12. The colour scales range from 1 to 5 kg.m^{-3} for density and from 60000 to 250000 Pa for pressure.

layers impinge on the plate and travel radially. Similar observations can be made for the pressure fields. In particular, for JetunderL4, concentric rings are visible in Figure 9(a,e). The rings are due to the dominant axisymmetric mode of the aeroacoustic feedback mechanism identified for this jet in Gojon *et al.*¹⁶ Indeed, at the frequency of the dominant resonant frequency, axisymmetrically organized turbulent structures are noticed in the jet shear layers.

IV.B.2. Pressure spectra

The pressure spectra obtained for the four ideally expanded jets are represented in Figure 10 as a function of the radial coordinate. The frequencies of the feedback mechanism all emerge between $r = 0$ and $r \approx 1.5r_0$, where the shear layers impinge on the plate, but only some of them remain visible for $r > 1.5r_0$, in the wall jet created after the impact. In the latter case, fewer tone frequencies appear for larger nozzle-to-plate distances.

In order to be more quantitative, the pressure spectra obtained at $r = 0$, $r = r_0$ and $r = 4r_0$ for the four ideally expanded jets are represented in Figure 11. As expected, because of the shear layer impingement, higher broadband levels are observed at $r = r_0$ than at the two other locations. The tone frequencies all appear at $r = 0$ and $r = r_0$, but only some of them are visible at $r = 4r_0$, for JetidealL6 and JetidealL8.

The pressure spectra obtained in the plate for the under-expanded jets are displayed in figure 12 as a function of the radial coordinate. As previously, the frequencies of the feedback mechanism are all visible between $r = 0.5r_0$ and $r \approx 1.5r_0$, but only some of them emerge for $r > 1.5r_0$. However, one clear difference

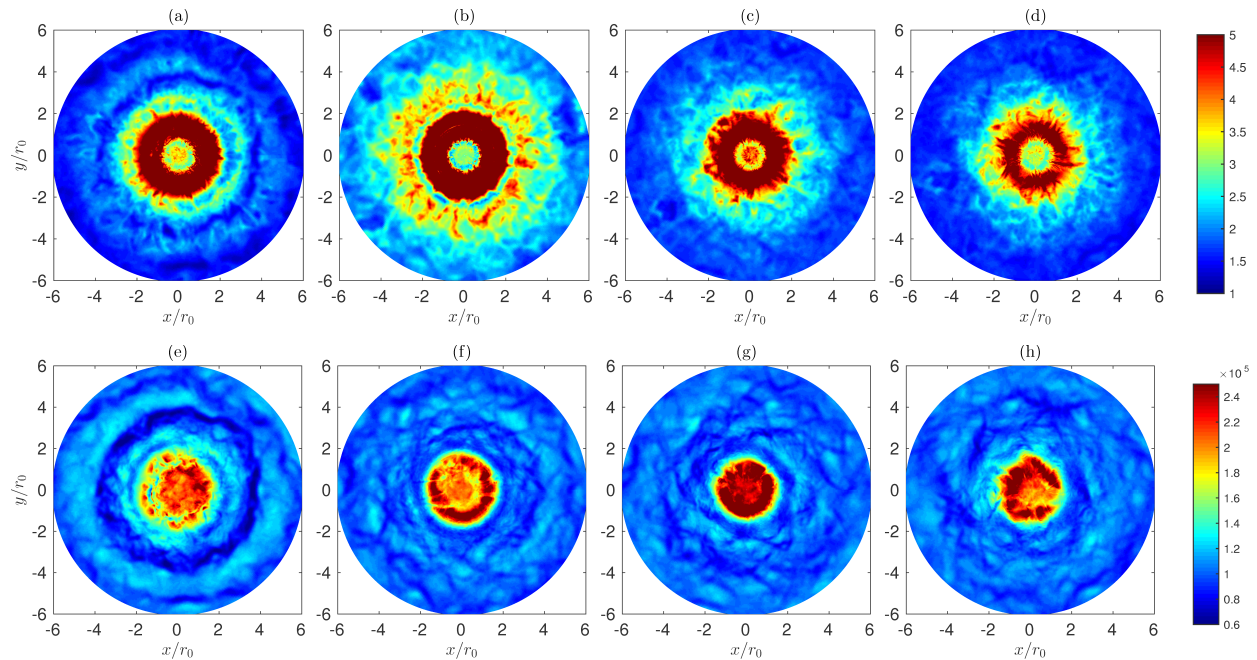


Figure 9. Density (top) and pressure (bottom) fields on the plate obtained for (a,e) JetunderL4, (b,f) JetunderL5, (c,g) JetunderL7 and (d,h) JetunderL9. The colour scales range from 1 to 5 $\text{kg}\cdot\text{m}^{-3}$ for density and from 60000 to 250000 Pa the pressure.

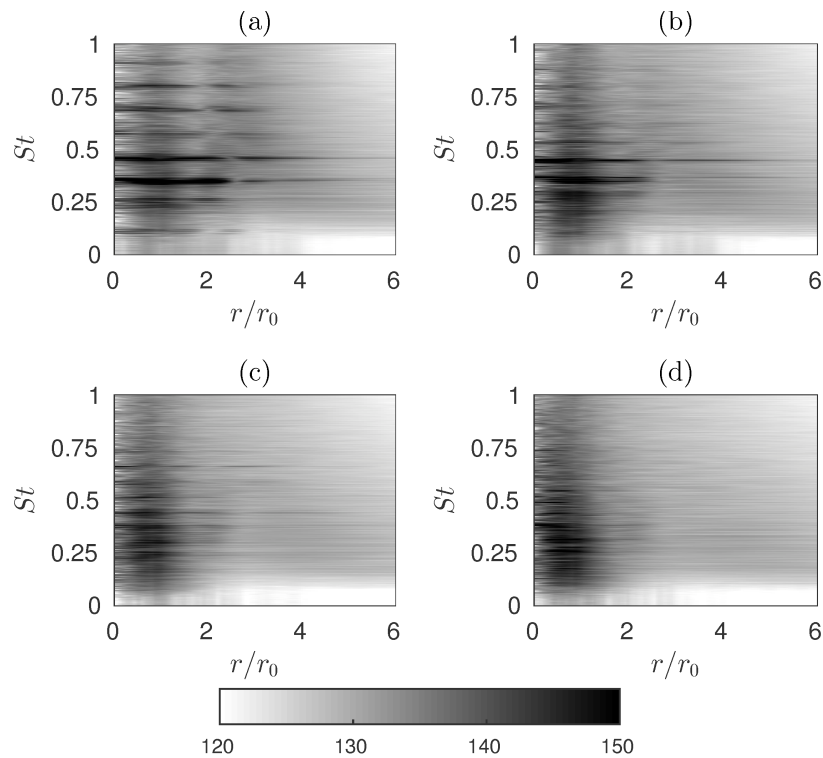


Figure 10. Pressure spectra obtained on the plate as functions of radial coordinate and Strouhal number for (a) JetidealL6, (b) JetidealL8, (c) JetidealL10 and (d) JetidealL12. The colour scale ranges from 120 to 150 dB/St .

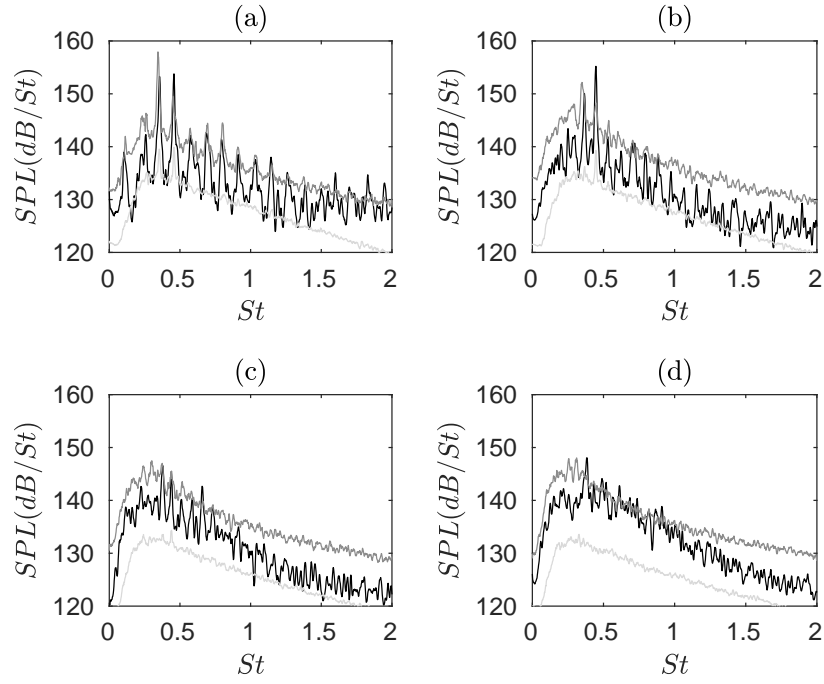


Figure 11. Pressure spectra obtained on the plate at $r = 0$, $r = r_0$ and $r = 4r_0$ as a function of Strouhal number for (a) JetidealL6, (b) JetidealL8, (c) JetidealL10 and (d) JetidealL12.

with respect to the ideally expanded jets is that for the most of the frequencies, the contribution seems negligible close to $r = 0$. Only one frequency, namely the main frequency of JetunderL4 at $St_2 = 0.505$, clearly appears in this region. This frequency corresponds to the only frequency associated with a strong motion of the near-wall Mach disk.¹⁶

The pressure spectra obtained at $r = 0$, $r = r_0$ and $r = 4r_0$ for the under-expanded jets are presented in figure 13. Similarly to the results for the ideally expanded jets, strong broadband components are found at $r = r_0$. All the feedback tone frequencies also emerge at this location. However, compared to the ideally expanded jets for which all the tone frequencies can be seen on the jet axis, only the dominant tone frequency of JetunderL4 at $St_2 = 0.505$ and its harmonics are visible at $r = 0$.

IV.B.3. Fourier decomposition

The amplitude and phase fields obtained for JetunderL4 at the two main tone frequencies at $St_1 = 0.375$ and $St_2 = 0.505$ are now presented in Figures 14 and 15, respectively.

The amplitude and phase fields of the fluctuating pressure obtained at $z = 0$ for $St_1 = 0.375$ are given in Figures 14(a,e). The amplitude field does not exhibit a clear pattern. On the contrary, the phase field shows two opposite regions out of phase on both sides of the jet axis followed by isophase contours of spiral shape. This indicates an helical organisation of the acoustic waves. In the plane $\theta = 0$, in the phase field of Figure 14(f), a 180-degree phase shift is visible with respect to the jet axis, suggesting a sinuous or helical oscillation mode of the jet. More precisely, from a Fourier decomposition of the fluctuating pressure in

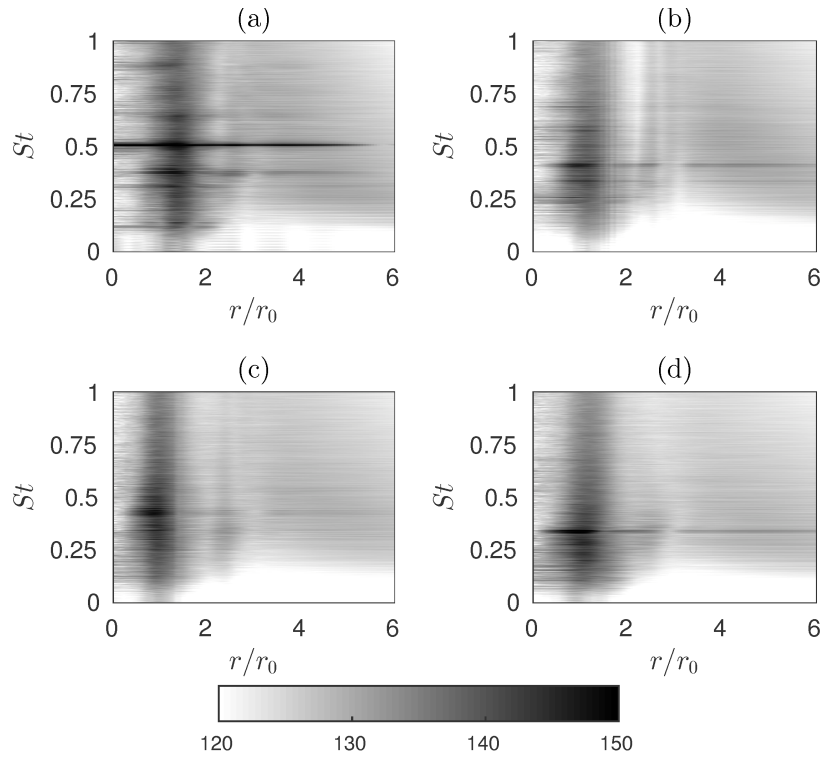


Figure 12. Pressure spectra obtained on the plate as functions of radial coordinate and Strouhal number for (a) JetunderL4, (b) JetunderL5, (c) JetunderL7 and (d) JetunderL9. The colour scale ranges from 120 to 150 dB/St.

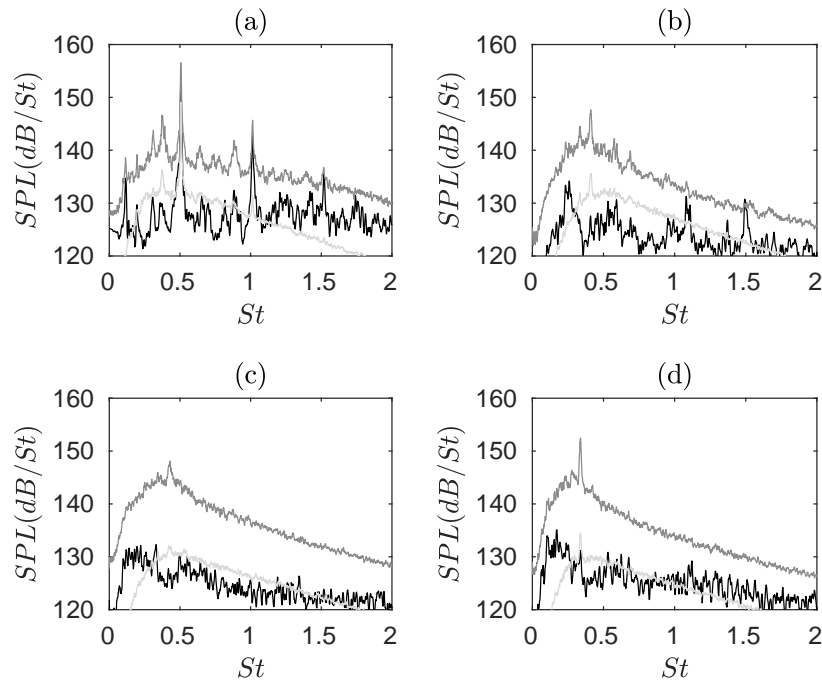


Figure 13. Pressure spectra obtained on the plate at $r = 0$, $r = r_0$ and $r = 4r_0$ as a function of Strouhal number for (a) JetunderL4, (b) JetunderL5, (c) JetunderL7 and (d) JetunderL9.

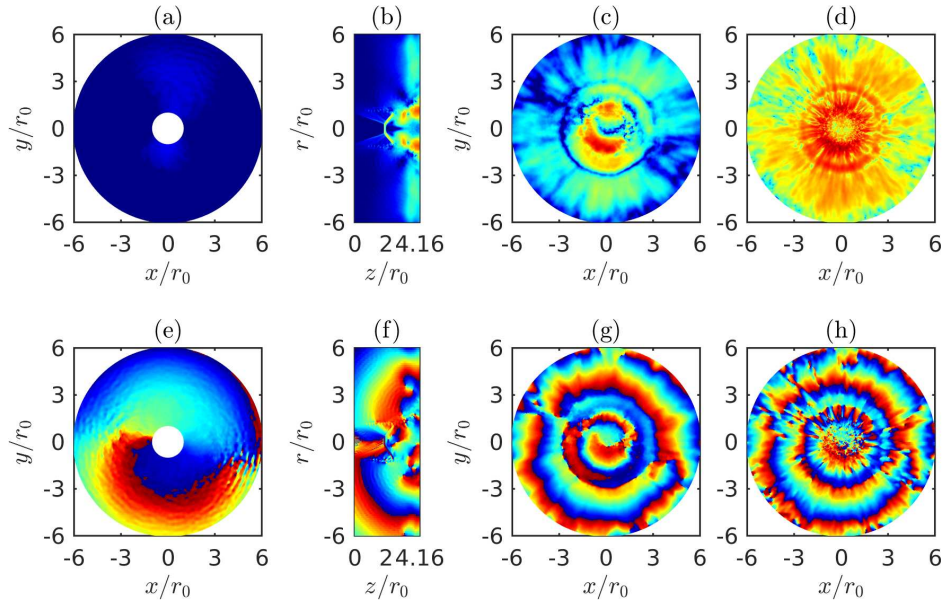


Figure 14. Amplitude (top) and phase (bottom) fields obtained for JetunderL4 at the tone frequency $St_1 = 0.375$; from pressure (a,e) at $z = 0$, (b,f) at $\theta = 0$ and (c,g) at $z = L$; from density (d,h) at $z = L$. The colour scales range from 120 to 160 dB/St for the amplitude fields of pressure, from 0 to 1 for the normalized amplitude field of density, and from $-\pi$ to π for the phase fields.

the azimuthal direction at $z = 0$ and $r = 2r_0$, the mode is helical. The amplitude and phase fields of the fluctuating pressure obtained on the plate are reported in Figures 14(c,g). The amplitude field reveals a region of high intensity for $r < 2.6r_0$ in the jet flow region. Looking at the amplitude field represented in Figure 14(b), this area is located downstream from the Mach disk and the annular oblique shock. The phase field, in Figure 14(g), shows a spiral which extends over the entire domain. The amplitude and phase fields of the fluctuating density on the plate are presented in Figures 14(d,h). They exhibit the same properties as those of the pressure fluctuations. The turbulent structures organized helically in the jet shear layers at the tone frequency $St_1 = 0.375$ impinge on the plate, and they seem to keep the same organization as they propagate radially on the plate.

The amplitude and phase fields of the fluctuating pressure and density determined for JetunderL4 at $St_2 = 0.505$, are represented in Figure 15. The results obtained at $z = 0$ for the pressure are given in Figures 15(a,e). The acoustic waves appear to be organized in an axisymmetric manner. The amplitude field in the plane $\theta = 0$ of Figure 15(b) reveals a cell structure between the nozzle and the plate, containing three cells. This structure is due to the generation of an hydrodynamic-acoustic standing wave by the aeroacoustic feedback mechanism. The number of cells in the standing wave is equal to the mode number of the feedback mechanism in the model of Ho & Nosseir,³ as shown by Gojon *et al.*³³ using a model of an hydrodynamic-acoustic standing wave proposed by Panda *et al.*³⁶ The phase field at $\theta = 0$, in Figure 15(f), exhibits a symmetric organisation with respect to the jet axis, corresponding to an axisymmetric oscillation mode. In Figures 15(g) and 15(h), concentric rings are observed in the phase fields of the fluctuating pressure

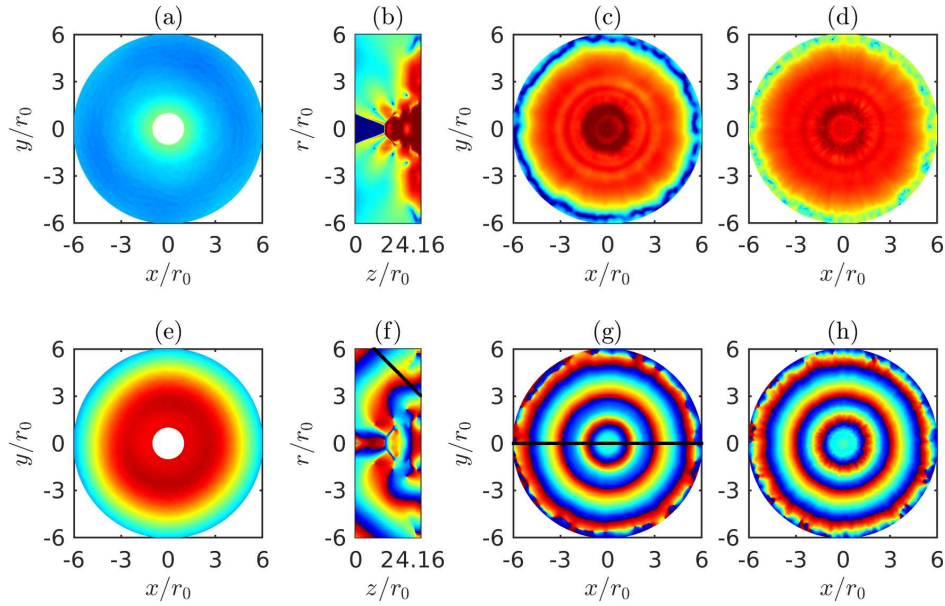


Figure 15. Amplitude (top) and phase (bottom) fields obtained for JetunderL4 at the dominant tone frequency $St_2 = 0.505$; from pressure (a,e) at $z = 0$, (b,f) at $\theta = 0$ and (c,g) at $z = L$; from density (d,h) at $z = L$. The colour scales range from 120 to 160 dB/St for the amplitude fields of pressure, from 0 to 1 for the normalized amplitude field of density, and from $-\pi$ to π for the phase fields.

and of the fluctuating density on the plate. These rings are probably due to the radial propagation, on the plate, of the coherent structures organised axisymmetrically in the jet shear layers.

In order to confirm the claims above, phase profiles are plotted in Figure 16. The profile in Figure 16(a) is that obtained in the $\theta = 0$ plane, along the black line visible in the phase field of Figure 15(f). It is represented in Figure 16(a) as a function of the distance l_{impact} from the point on the wall at $z = 3r_0$. This point is chosen since it corresponds approximately to the location of the source of the acoustic component radiating in the far field, see in Henderson *et al.*⁷ and in Gojon *et al.*¹⁶ The maxima in the phase profile are located at $l_{impact} = r_0, 4.25r_0$ and $7.6r_0$, giving wavelengths of $3.25r_0$ and $3.35r_0$, hence phase speeds of 327 m.s^{-1} and 338 m.s^{-1} , respectively. These velocities are close to the ambient sound speed, as expected for acoustic waves. In Figure 16(b), the phase profile obtained in the $z = L$ plane along the black line shown in Figure 15(g) is depicted as a function of the radial coordinate. The wavelengths of the concentric rings apparent in Figures 15(g,h) can thus be measured. They are equal to $1.75r_0$ between the first and the second maxima and to $2.15r_0$ between the second and the third maxima, yielding phase speeds of $0.40u_j$ and $0.49u_j$, respectively. Therefore, the pressure and density patterns obtained at the wall cannot be due to acoustic waves, but are associated with the radial convection of turbulent structures in the wall jets. Thus, for the non-ideally expanded jets, the temporal organization of the wall jet along the frequencies of the feedback mechanism seems to be linked to the oscillations of the Mach disk located just upstream of the plate. Indeed, for JetunderL4, the Mach disk located just upstream of the plate strongly oscillates at $St_2 = 0.505$.¹⁶ A movie given in a previous paper¹⁶ allows us to see the Mach disk pumping and forcing

the turbulent structure to stay organized from the jet shear layers to the wall jet. Finally, it is interesting to note that the two tone frequencies of JetunderL4 are produced simultaneously,¹⁶ the axisymmetrical and the spiral organizations of the wall jet are thus establishing at the same time.

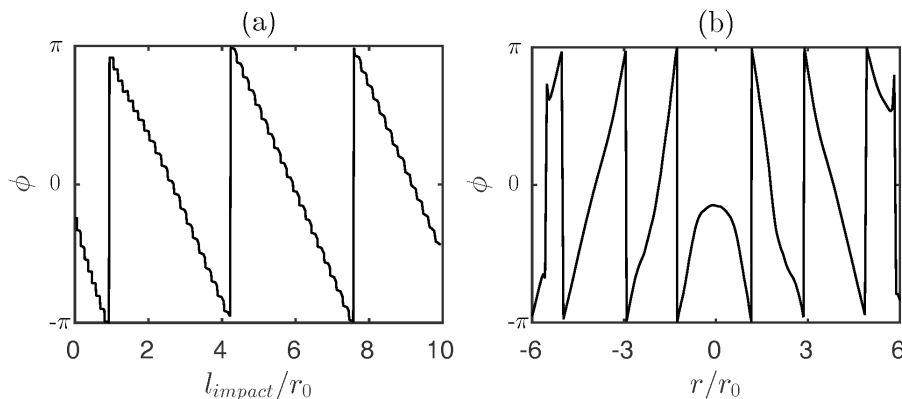


Figure 16. Phase profiles obtained for JetunderL4 at $St_2 = 0.505$, (a) in the plane $\theta = 0$ along the black line represented in Figure 15(f), and (b) at $z = L$ along the black line in Figure 15(g).

For the ideally expanded jet JetidealL6, the results obtained at the main tone frequency at $St_3 = 0.455$ are represented in Figure 17. The amplitude field at $\theta = 0$ of Figure 17(b) reveals a cell structure between the nozzle and the plate, containing four cells. This structure is due to the generation of an hydrodynamic-acoustic standing wave by the aeroacoustic feedback mechanism, and the number of cells is equal to the mode number of the feedback mechanism.³³ Moreover, a symmetric organisation with respect to the jet axis appears in the phase field of Figure 17(f). The jet thus undergoes an axisymmetric oscillation at $St_3 = 0.455$. In Figures 17(g) and 17(h), concentric rings are observed in the phase fields of the fluctuating pressure and density on the plate. These rings result from the radial propagation, on the plate, of the coherent structures organised axisymmetrically in the jet shear layers.

IV.B.4. Convection velocity of the turbulent structures in the wall jets

In order to give further insight into the convection velocity of the structures in the wall jets in all cases, the pressure phase fields on the plate are investigated in the same way as for JetunderL4 in Figure 16(b). First, let us consider two regions of interest. The first one is near the jet axis over $0 < r < 3r_0$, and the second one is several diameters away over $3r_0 < r < 6r_0$. The mean wavelengths are extracted from the phase profiles in each of the two regions and the corresponding convection velocities are given in Table 4.

Over $3r_0 < r < 6r_0$, the convection velocity of the turbulent structures on the wall varies between $0.40u_j$ and $0.49u_j$ and no clear distinctions can be made between the ideally-expanded jets and the under-expanded ones. The results are in agreement with the measurements of Davis *et al.*¹⁵ for ideally expanded impinging round jets, who found a convection velocity on the wall equal to $0.47u_j$ several diameters away from the

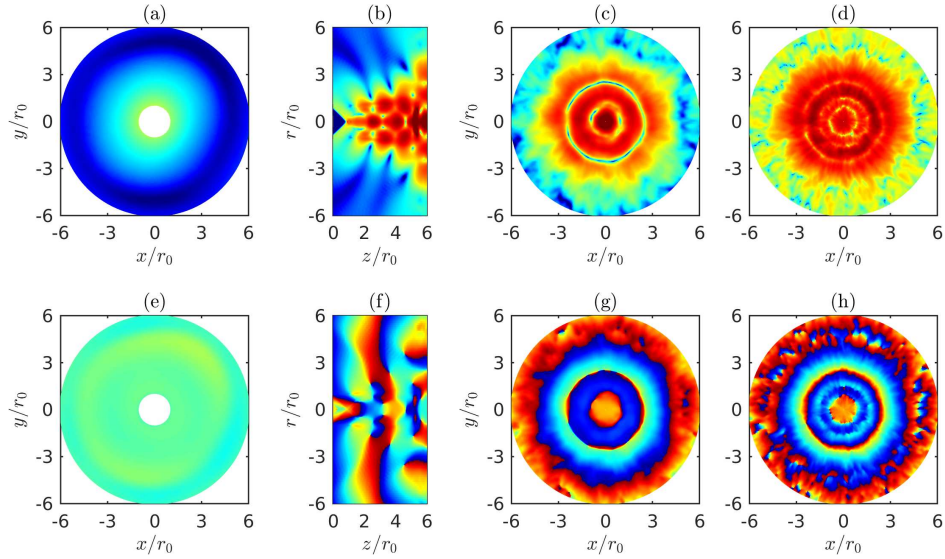


Figure 17. Amplitude (top) and phase (bottom) fields obtained for JetidealL6 at the tone frequency $St_3 = 0.455$; from pressure (a,e) at $z = 0$, (b,f) at $\theta = 0$ and (c,g) at $z = L$; from density (d,h) at $z = L$. The colour scales range from 120 to 160 dB/St for the amplitude fields of pressure, from 0 to 1 for the normalized amplitude field of density, and from $-\pi$ to π for the phase fields.

Jet	St	$u_c (0 < r < 3r_0)$	$u_c (3r_0 < r < 6r_0)$
JetidealL6	$St_2 = 0.345$	$u_c = 0.57u_j$	$u_c = 0.49u_j$
JetidealL6	$St_3 = 0.455$	$u_c = 0.54u_j$	$u_c = 0.47u_j$
JetidealL8	$St_4 = 0.445$	$u_c = 0.51u_j$	$u_c = 0.45u_j$
JetidealL10	$St_4 = 0.44$	$u_c = 0.49u_j$	$u_c = 0.43u_j$
JetidealL12	$St_4 = 0.38$	$u_c = 0.45u_j$	$u_c = 0.41u_j$
JetunderL4	$St_1 = 0.375$	$u_c = 0.27u_j$	$u_c = 0.40u_j$
JetunderL4	$St_2 = 0.505$	$u_c = 0.40u_j$	$u_c = 0.49u_j$
JetunderL5	$St_2 = 0.415$	$u_c = 0.35u_j$	$u_c = 0.47u_j$
JetunderL7	$St_2 = 0.345$	$u_c = 0.38u_j$	$u_c = 0.48u_j$
JetunderL9	$St_2 = 0.34$	$u_c = 0.34u_j$	$u_c = 0.46u_j$

Table 4. Mean convection velocities of the turbulent structures in the wall jets for different main tone frequencies.

jet axis by using Pressure-Sensitive Paint on the flat plate. The results are also consistent with the mean convection velocity of the tubulent structures in the jet shear layers, which is between $0.54u_j$ and $0.59u_j$ for the four under-expanded jets.¹⁶

Over $0 < r < 3r_0$, the convection velocity of the turbulent structures on the wall varies between $0.27u_j$ and $0.57u_j$. These values are in agreement with the value of $0.56u_j$ found experimentally by Davis *et al.*¹⁵ in this region for ideally expanded impinging round jets. The convection velocities are between $0.45u_j$ and $0.57u_j$ for the ideally expanded jets, but between $0.27u_j$ and $0.40u_j$ for the non-ideally expanded jets. This difference is likely caused by the presence of a Mach disk in the near-wall region for the non-ideally jets, as observed in Figure 6. The jet shear layers are thus deviated and impinge on the plate at $r \simeq 2r_0$. Consequently, the mean convection velocities computed near the jet axis does not correspond to the convection velocity of the turbulent structures, as the motion of these structures is not only radial in this region. On the contrary,

in the ideally expanded jets, the turbulent structures in the jet shear layers impinge near the jet axis as illustrated by Krothapalli *et al.*⁶ and Davis *et al.*¹⁵ and observed in Figure 4. Finally, it is interesting to note that for JetunderL4, in the region $3r_0 < r < 6r_0$, the convection velocity of the structures organised axisymmetrically at the tone frequency $St_2 = 0.505$ is 22.5% higher than the the convection velocity of the turbulent structures organised helically at $St_1 = 0.375$.

The convection velocity in the wall jets is now computed from radial velocity cross-correlations just upstream from the wall, at a fixed wall-normal position of $0.1r_0$. This position has been chosen for two reasons. First, it is difficult to follow the position of maximum rms velocity, as it is usually done to compute the convection velocity of the turbulent structures in the shear-layers^{37,38} in free jets, because of the complex flow patterns that arise near the jet axis, notably for the non-ideally expanded jets, see in Figure 7. Then, in order to compare the results with those obtained experimentally using pressure sensitive paint and those of the present paper from pressure phase fields on the plate, the convection velocity needs to be computed very close to the wall. The results are represented in Figure 18(a) for the ideally expanded jets and in Figure 19(a) for the non-ideally expanded jets as a function of the radial position between $r = 0$ and $r = 6r_0$. The maximal mean radial velocity in the wall jets is also provided in Figures 18(b) and 19(b). This velocity correspond to the signed velocity where the absolute value of the radial velocity is maximal in the wall jet, permitting also to look at recirculation region. For the ideally expanded jets, in Figure 18(a), the convection velocity increases from 0 to about $0.55u_j$ from $r = 0$ to $r = 2.5r_0$. It then decreases slowly in the region $r \geq 2.5r_0$ to reach $0.38r_0$ at $r = 6r_0$. These result are in good agreement with the convection velocities obtained from the phase profiles in Table 4 and with those measured in the phase averaged distributions of the fluctuating pressure of the ideally expanded jets of Davis *et al.*¹⁵

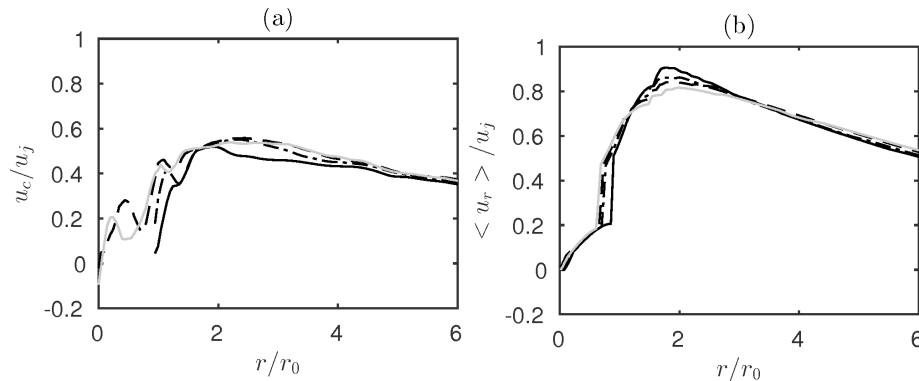


Figure 18. Variation with the radial distance of (a) the convection velocity computed from the cross-correlations of radial velocity fluctuations just upstream from the wall and (b) the maximal mean radial velocity in the wall jet for **—** JetidealL6, **- - -** JetidealL8, **- · - ·** JetidealL10, and **— — —** JetidealL12.

For the non-ideally expanded jets, in Figure 19(a), a region of negative convection velocity appears around $r = r_0$ for JetunderL4, JetunderL5 and JetunderL7. This is due to the presence of a recirculation bubble near the region of impact, observed experimentally for similar jets by Krothapalli *et al.*⁶ This recirculation zone

leads in Figure 19(b) to a negative mean radial velocity for $r < r_0$. It explains the difference between the convection velocities previously noticed over $0 < r < 3r_0$ for the under-expanded and the ideally expanded jets. A peak convection velocity between $0.45u_j$ and $0.5u_j$ is then reached at $r \sim 3r_0$ before a slow decrease in the region $r \geq 3r_0$ to reach values between $0.44u_j$ and $0.69u_j$ at $r = 6r_0$.

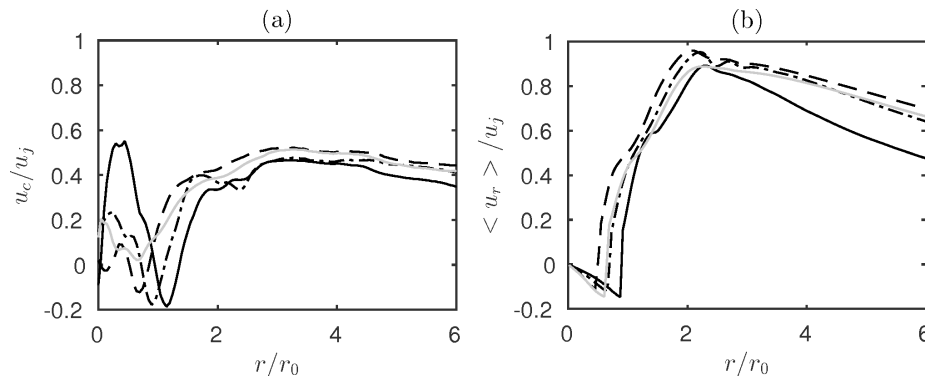


Figure 19. Variation with the radial distance of (a) the convection velocity computed from the cross-correlations of radial velocity fluctuations just upstream from the wall and (b) the maximal radial velocity in the wall jet for — JetunderL4, - - JetunderL5, - · - JetunderL7, and - - - JetunderL9.

The maximal radial velocity in the wall jet is higher in the non-ideally expanded jets than in the ideally expanded ones, but the opposite trend is noted for the convection velocity.

V. Conclusion

In this paper, the flow properties near the flat plate for ideally expanded and non-ideally expanded impinging round jets have been studied using compressible large eddy simulation. They have been characterized in the jet shear layers but also on the flat plate, in order to examine the wall jets created after the jet impact. For all jets, the spectra in the near pressure fields revealed several tone frequencies due to a feedback mechanism occurring between the nozzle lips and the flat plate. The near pressure and density fields of the jets are then analyzed using Fast Fourier Transform on the nozzle exit plane, the plate plane and an azimuthal plane. It is found that the helical or axisymmetric organization of the turbulent structures in the jet shear layers, specific to each tone frequency, persists after the jet impact on the plate. The radial propagation of these structures in the wall jets leads to a spiral or to concentric rings in the phase fields, respectively. In particular, for one of the jets, a spiral shape and concentric rings are observed at two different tone frequencies. Finally, the convection velocity of the turbulent structures in the wall jets is evaluated from the phase fields and cross-correlations of radial velocity. Over $3r_0 < r < 6r_0$, the convection velocity of the structures varies between $0.40u_j$ and $0.49u_j$ in the present jets. These results are in agreement with measurements for supersonic impinging round jets performed using Pressure-Sensitive Paint on the flat plate. Near the jet axis, differences are observed between the ideally expanded jets and the non-ideally expanded ones with

negative convection velocities found around the lip-line radial position in the latter case. Finally, for the non-ideally expanded jets, the temporal organization of the wall jet along the frequencies of the feedback mechanism seems to be linked to the oscillation of the Mach disk located just upstream of the plate, pumping and forcing the turbulent structure to stay organized from the jet shear layers to the wall jet.

Acknowledgments

The simulations presented in the paper were performed using the High-Performance-Computing resources of FLMSN (Fédération Lyonnaise de Modélisation et Sciences Numériques), partner of EQUIPEX EQUIP@MESO and of CINES (Centre Informatique National de l'Enseignement Supérieur) under the allocation 2016-2a0204 made by GENCI (Grand Equipement National de Calcul Intensif). This work was performed within the framework of the Labex CeLyA of Université de Lyon, within the program "Investissements d'Avenir" (ANR-10-LABX-0060/ ANR-11-IDEX-0007) operated by the French National Research Agency (ANR).

References

- ¹A. Powell, "On edge tones and associated phenomena," *Acta Acustica united with Acustica*, vol. 3, pp. 233–243, 1953.
- ²F. Wagner, "The sound and flow field of an axially symmetric free jet upon impact on a wall," *NASA*, vol. NASA TT F-13942, 1971.
- ³C. Ho and N. Nosseir, "Dynamics of an impinging jet. part 1. The feedback phenomenon," *Journal of Fluid Mechanics*, vol. 105, pp. 119–142, 1981. doi: 10.1017/S0022112081003133.
- ⁴N. Nosseir and C. Ho, "Dynamics of an impinging jet. part 2. The noise generation," *Journal of Fluid Mechanics*, vol. 116, pp. 379–391, 1982. doi: 10.1017/S0022112082000512.
- ⁵B. Henderson and A. Powell, "Experiments concerning tones produced by an axisymmetric choked jet impinging on flat plates," *Journal of Sound and Vibrations*, vol. 168, no. 2, pp. 307–326, 1993. doi: 10.1006/jsvi.1993.1375.
- ⁶A. Krothapalli, E. Rajkuperan, F. Alvi, and L. Lourenco, "Flow field and noise characteristics of a supersonic impinging jet," *Journal of Fluid Mechanics*, vol. 392, pp. 155–181, 1999. doi: 10.1017/S0022112099005406.
- ⁷B. Henderson, J. Bridges, and M. Wernet, "An experimental study of the oscillatory flow structure of tone-producing supersonic impinging jets," *Journal of Fluid Mechanics*, vol. 542, pp. 115–137, 2005. doi: 10.1017/S0022112005006385.
- ⁸A. Risborg and J. Soria, "High-speed optical measurements of an underexpanded supersonic jet impinging on an inclined plate," *28th International Congress on High-Speed Imaging and Photonics*, vol. 7126, no. F, 2009. doi: 10.1117/12.822137.
- ⁹N. Buchmann, D. Mitchell, K. Ingvorsen, D. Honnery, and J. Soria, "High spatial resolution imaging of a supersonic under-expanded jet impinging on a flat plate," *6th Australian Conference on Laser Diagnostics in Fluid Mechanics and Combustion*, 2011.
- ¹⁰D. Mitchell, D. Honnery, and J. Soria, "The visualization of the acoustic feedback loop in impinging underexpanded

supersonic jet flows using ultra-high frame rate schlieren,” *Journal of visualization*, vol. 15, no. 4, pp. 333–341, 2012. doi: 10.1007/s12650-012-0139-9.

¹¹C. Kuo and A. Dowling, “Oscillations of a moderately underexpanded choked jet impinging upon a flat plate,” *Journal of Fluid Mechanics*, vol. 315, pp. 267–291, 1996. doi: 10.1017/S002211209600242X.

¹²A. Dauplain, B. Cuenot, and L. Gicquel, “Large eddy simulation of stable supersonic jet impinging on flat plate,” *AIAA Journal*, vol. 48, no. 10, pp. 2325–2338, 2010. doi: 10.2514/1.J050362.

¹³A. Dauplain, L. Gicquel, and S. Moreau, “Large eddy simulation of supersonic impinging jets,” *AIAA Journal*, vol. 50, no. 7, pp. 1560–1574, 2012. doi: 10.2514/1.J051470.

¹⁴J. Weightman, O. Amili, D. Honnery, J. Soria, and D. Edgington-Mitchell, “An explanation for the phase lag in supersonic jet impingement,” *Journal of Fluid Mechanics*, vol. 815, 2017. doi: 10.1017/jfm.2017.37.

¹⁵T. Davis, A. Edstrand, F. Alvi, L. Cattafesta, D. Yorita, and K. Asai, “Investigation of impinging jet resonant modes using unsteady pressure-sensitive paint measurements,” *Experiments in Fluids*, vol. 56, no. 5, pp. 1–13, 2015. doi: 10.1007/s00348-015-1976-9.

¹⁶R. Gojon and C. Bogey, “Flow structure oscillations and tone production in underexpanded impinging round jets,” *AIAA Journal*, vol. 55, no. 6, pp. 1792–1805, 2017. doi: 10.2514/1.J055618.

¹⁷C. Bogey and R. Gojon, “Feedback loop and upwind-propagating waves in ideally-expanded supersonic impinging round jets,” *Journal of Fluid Mechanics*, vol. 823, pp. 562–591, 2017. doi: 10.1017/jfm.2017.334.

¹⁸C. Bogey and C. Bailly, “A family of low dispersive and low dissipative explicit schemes for flow and noise computations,” *Journal of Computational Physics*, vol. 194, no. 1, pp. 194–214, 2004. doi: 10.1016/j.jcp.2003.09.0.

¹⁹J. Berland, C. Bogey, O. Marsden, and C. Bailly, “High-order, low dispersive and low dissipative explicit schemes for multiple-scale and boundary problems,” *Journal of Computational Physics*, vol. 224, no. 2, pp. 637–662, 2007. doi: 10.1016/j.jcp.2006.10.017.

²⁰C. Bogey and C. Bailly, “Large eddy simulations of transitional round jets: influence of the Reynolds number on flow development and energy dissipation,” *Physics of Fluids*, vol. 18, p. 065101, 2006. doi: 10.1063/1.2204060.

²¹C. Bogey and C. Bailly, “Turbulence and energy budget in a self-preserving round jet: direct evaluation using large eddy simulation,” *Journal of Fluid Mechanics*, vol. 627, pp. 129–160, 2009. doi: 10.1017/S0022112009005801.

²²D. Fauconnier, C. Bogey, and E. Dick, “On the performance of relaxation filtering for large-eddy simulation,” *Journal of Turbulence*, vol. 14, no. 1, pp. 22–49, 2013. doi: 10.1080/14685248.2012.740567.

²³C. Tam and Z. Dong, “Wall boundary conditions for high-order finite-difference schemes in computational aeroacoustics,” *Theoretical and Computational Fluid Dynamics*, vol. 6, pp. 303–322, 1994. doi: 10.1007/BF00311843.

²⁴C. Bogey, N. de Cacqueray, and C. Bailly, “A shock-capturing methodology based on adaptive spatial filtering for high-order non-linear computations,” *Journal of Computational Physics*, vol. 228, no. 5, pp. 1447–1465, 2009. doi: 10.1016/j.jcp.2008.10.042.

²⁵K. Mohseni and T. Colonius, “Numerical treatment of polar coordinate singularities,” *Journal of Computational Physics*, vol. 157, no. 2, pp. 787–795, 2000. doi: 10.1006/jcph.1999.6382.

²⁶C. Bogey, N. de Cacqueray, and C. Bailly, “Finite differences for coarse azimuthal discretization and for reduction of effective resolution near origin of cylindrical flow equations,” *Journal of Computational Physics*, vol. 230, no. 4, pp. 1134–1146, 2011. doi: 10.1016/j.jcp.2010.10.031.

²⁷C. Bogey, O. Marsden, and C. Bailly, “Large-eddy simulation of the flow and acoustic fields of a Reynolds number 10^5 subsonic jet with tripped exit boundary layers,” *Physics of Fluids*, vol. 23, p. 035104, 2011. doi: 10.1063/1.3555634.

²⁸S. Viazzo, A. Dejoan, and R. Schiestel, “Spectral features of the wall-pressure fluctuations in turbulent wall flows with

and without perturbations using les,” *International Journal of Heat and Fluid Flow*, vol. 22, no. 1, pp. 39–52, 2001. doi: 10.1016/S0142-727X(00)00074-6.

²⁹X. Gloerfelt and J. Berland, “Direct computation of turbulent boundary layer noise,” *AIAA Paper*, vol. 2009-3401, pp. 1–22, 2009. doi: 10.2514/6.2009-3401.

³⁰P. Schlatter, Q. Li, G. Brethouwer, A. Johansson, and D. Henningson, “Simulations of spatially evolving turbulent boundary layers up to $Re_\theta = 4300$,” *International Journal of Heat and Fluid Flow*, vol. 31, no. 3, pp. 251–261, 2010. doi: 10.1016/j.ijheatfluidflow.2009.12.011.

³¹C. Bogey and O. Marsden, “Simulations of initially highly disturbed jets with experiment-like exit boundary layers,” *AIAA Journal*, vol. 54, no. 2, pp. 1299–1312, 2016. doi: 10.2514/1.J054426.

³²T. Norum, “Supersonic rectangular jet impingement noise experiments,” *AIAA Journal*, vol. 29, no. 7, pp. 1051–1057, 1991. doi: 10.2514/3.10703.

³³R. Gojon, C. Bogey, and O. Marsden, “Investigation of tone generation in ideally expanded supersonic planar impinging jets using large-eddy simulation,” *Journal of Fluid Mechanics*, vol. 808, pp. 90–115, 2016. doi: 10.1017/jfm.2016.628.

³⁴A. Powell, “The sound-producing oscillations of round underexpanded jets impinging on normal plates,” *The Journal of the Acoustical Society of America*, vol. 83, no. 2, pp. 515–533, 1988. doi: 10.1121/1.396146.

³⁵B. Henderson, “The connection between sound production and jet structure of the supersonic impinging jet,” *The Journal of the Acoustical Society of America*, vol. 111, no. 2, pp. 735–747, 2002. doi: 10.1121/1.1436069.

³⁶J. Panda, G. Raman, and K. Zaman, “Underexpanded screeching jets from circular, rectangular and elliptic nozzles,” *AIAA Paper 97-1623*, 1997. doi: 10.2514/6.1997-1623.

³⁷B. André, *Etude expérimentale de l’effet du vol sur le bruit de choc de jets supersoniques sous-détendus*. PhD thesis, Ecole Centrale de Lyon, NNT: 2012ECDL0042, 2012.

³⁸R. Gojon and C. Bogey, “Simulations of initially highly disturbed jets with experiment-like exit boundary layers,” *International Journal of Aeroacoustics*, to appear, 2017. doi: 10.1177/1475472X17727606.